

Insight into Interfacial Heat Transfer of β -Ga₂O₃/Diamond Heterostructures via the Machine Learning Potential

Zhanpeng Sun^{1,2,#}, Dongliang Zhang^{3,#}, Zijun Qi^{1,2}, Qijun Wang^{1,2}, Xiang Sun^{1,2}, Kang Liang^{1,2},
Fang Dong^{1,2,4}, Yuan Zhao², Diwei Zou², Lijie Li⁵, Gai Wu^{1,2,4,*}, Wei Shen^{1,2,4,*}, Sheng Liu^{1,2,3}

¹ The Institute of Technological Sciences, Wuhan University, Wuhan 430072, China

² School of Power and Mechanical Engineering, Wuhan University, Wuhan 430072, China

³ School of Mechanical Science and Engineering, Huazhong University of Science and Technology,
Wuhan 430074, China

⁴ Hubei Key Laboratory of Electronic Manufacturing and Packaging Integration, Wuhan University,
Wuhan 430072, China

⁵ College of Engineering, Swansea University, Swansea SA1 8EN, UK

* Corresponding Authors:

Gai Wu, E-mail: wugai1988@whu.edu.cn

Wei Shen, E-mail: wei_shen_@whu.edu.cn

Zhanpeng Sun and Dongliang Zhang contributed equally to this work.

ABSTRACT

β -Ga₂O₃ is an ultrawide-bandgap semiconductor with excellent potential for high-power and ultraviolet optoelectronic device applications. The low thermal conductivity is one of the major obstacles to enable the full performance of the β -Ga₂O₃-based devices. A promising solution for this problem is to integrate β -Ga₂O₃ with the diamond heat sink. However, the thermal properties of the β -Ga₂O₃/diamond heterostructures after the interfacial bonding have not been studied extensively, which are influenced by the crystal orientations and the interfacial atoms for the β -Ga₂O₃ and diamond interfaces. In this work, the molecular dynamics simulations based on the machine learning potential have been adopted to investigate the crystal-orientation-dependent and interfacial-atom-dependent thermal boundary resistance (TBR) of the β -Ga₂O₃/diamond heterostructure after the interfacial bonding. The differences in TBR at different interfaces are explained in detail through the explorations of thermal conductivity value, thermal conductivity spectra, vibration density of states and interfacial structures. Based on the above explorations, further understandings of the influence of different crystal orientations and interfacial atoms on the β -Ga₂O₃/diamond heterostructure were conducted. Finally,

the insightful optimization strategies have been proposed in the study which could pave the way for better thermal design and management of β -Ga₂O₃/diamond heterostructures according to the guidance in the selection of the crystal orientations and interfacial atoms of the β -Ga₂O₃ and diamond interfaces.

Keywords: β -Ga₂O₃/diamond heterostructure, Interfacial heat transfer, Molecular dynamics, Machine learning potential, Thermal boundary resistance

1. Introduction

β -Ga₂O₃ is regarded as a potential candidate for next-generation power devices due to the wide band gap of ~ 4.9 eV and high breakdown electric field of $8 \text{ MV}\cdot\text{cm}^{-1}$.¹⁻⁴ The major barrier to the realization of high-power β -Ga₂O₃ devices lies in the low thermal conductivity of $\sim 10\text{--}29 \text{ W}\cdot\text{m}^{-1}\cdot\text{K}^{-1}$,^{5,6} which usually results in heat dissipation issues. An excellent solution is the integration of the high thermal conductivity materials with the low ones to enhance the heat dissipation.⁷⁻¹⁰ Diamond is a well-recognized promising candidate ($>2000 \text{ W}\cdot\text{m}^{-1}\cdot\text{K}^{-1}$)¹¹⁻¹⁴ for the integration with β -Ga₂O₃. For example, Kim et al. adhered n-type β -Ga₂O₃ to p-type diamond through van der Waals interactions and achieved a p-n junction photodiode, due to the most important factor that diamond nearly boasts the greatest heat dissipation properties compared with other materials.¹⁵ The thermal conductivity of the β -Ga₂O₃/diamond van der Waals heterogeneous interface has been analyzed in experiment, which could confirm that the heat dissipation performance of Ga₂O₃-devices could be significantly improved via the integration of diamond heat sink.¹⁶ It is noteworthy that Matsumae et al. achieved the β -Ga₂O₃/diamond heterostructure by low-temperature direct bonding of β -Ga₂O₃ and diamond substrate under atmospheric conditions.^{17, 18} Sittimart et al. reported that the electrical performance of diamond/ β -Ga₂O₃ p-n heterojunction diodes fabricated by the interfacial bonding was better than that prepared by van der Waals.¹⁹ In addition, Graham et al. reported that the thermal boundary resistance of β -Ga₂O₃/diamond heterostructure adhered by van der Waals interactions is 10 times larger than that of interfacial bonding.²⁰ Therefore, the interfacial bonding of β -Ga₂O₃ and diamond is extremely important, especially for the thermal management.²¹ However, for the moment, there have been few explorations of the interfacial heat transfer for the diamond/ β -Ga₂O₃ heterostructures after the interfacial bonding, especially for the consideration of the influence of different crystal orientations and interfacial atoms at the β -Ga₂O₃ and diamond interfaces.

Molecular dynamics (MD) simulations have been widely applied to investigate the interfacial thermal transport properties of the heterostructures.²²⁻²⁴ One of the obvious disadvantages for MD simulations is that it relies heavily on the accurate interatomic potentials. Unfortunately, the high-accuracy empirical potential of

Ga₂O₃ is currently lacking, which is difficult to be obtained.²⁵ It is particularly challenging to obtain an empirical potential that can accurately describe Ga₂O₃ and diamond at the same time, such as the β -Ga₂O₃/diamond heterostructure. Although Xin et al. have explored the interfacial heat transfer of graphene/ β -Ga₂O₃ based on its self-consistent interatomic potential,²⁶ whether it can be accurately applied to the interfacial heat transfer of β -Ga₂O₃/diamond remains to be verified.²⁷

Recent research efforts have been taken in the thermal transport investigation based on machine learning (ML).^{28, 29} In this approach, the *ab initio* potential energy surface was reconstructed via ML to obtain an accurate interatomic potential. Utilizing the ML potential, other groups have recently discussed the thermal properties of graphene/borophene,³⁰ Ge/GaAs,³¹ and so on. Compared with other ML algorithms, the neuroevolution potential (NEP) obtained through Graphics Processing Units Molecular Dynamics code (GPUMD)³²⁻³⁴ has high accuracy and low cost in atomistic simulations and heat transport applications.³⁵

In this work, the TBR of the β -Ga₂O₃/diamond interfaces were investigated. The effects of crystal orientations and interfacial atoms of β -Ga₂O₃/diamond interfaces were studied from the perspectives of thermal conductivity value, thermal conductivity spectra, vibration density of states and interfacial structures, which could thus provide insightful optimization strategies and pave the way for better thermal design and management of β -Ga₂O₃/diamond heterostructures according to the guidance in the selection of the crystal orientations and interfacial atoms of the β -Ga₂O₃ and diamond interfaces. The software used to train the machine learning potentials and perform the molecular dynamics simulations was GPUMD-3.6.

2. Computational methods and models

2.1 Brief introduction to the NEP method

The NEP model is a machine learning potential (MLP) based on a single neural network, which is trained using a separable natural evolution strategy.³⁶ The NEP model derives the potential energy surface function U_i for atom i by modeling the descriptor vector q_v^i , which can be determined by the following formula^{35, 37, 38}:

$$U_i = \sum_{\mu=1}^{N_{neu}} \omega_{\mu}^{(1)} \tanh \left(\sum_{v=1}^{N_{des}} \omega_{\mu v}^{(0)} q_v^i - b_{\mu}^{(0)} \right) - b^{(1)} \quad (1)$$

where N_{des} is the number of components of the descriptor vector, N_{neu} is the number of neurons, $\tanh(x)$ is the activation function of the hidden layer, $\omega^{(0)}$ is the matrix of connection weights from the input layer to the hidden layer, $\omega^{(1)}$ is the vector of connection weights from the hidden layer to the output layer node U_i , $b^{(0)}$ is

the bias vector of the hidden layer, and $b^{(1)}$ is the bias of the output layer node U_i . As depicted in Fig. 1(a), NEP has three layers: the input, the hidden, and the output layers. The hidden layer in this study has 60 neurons.

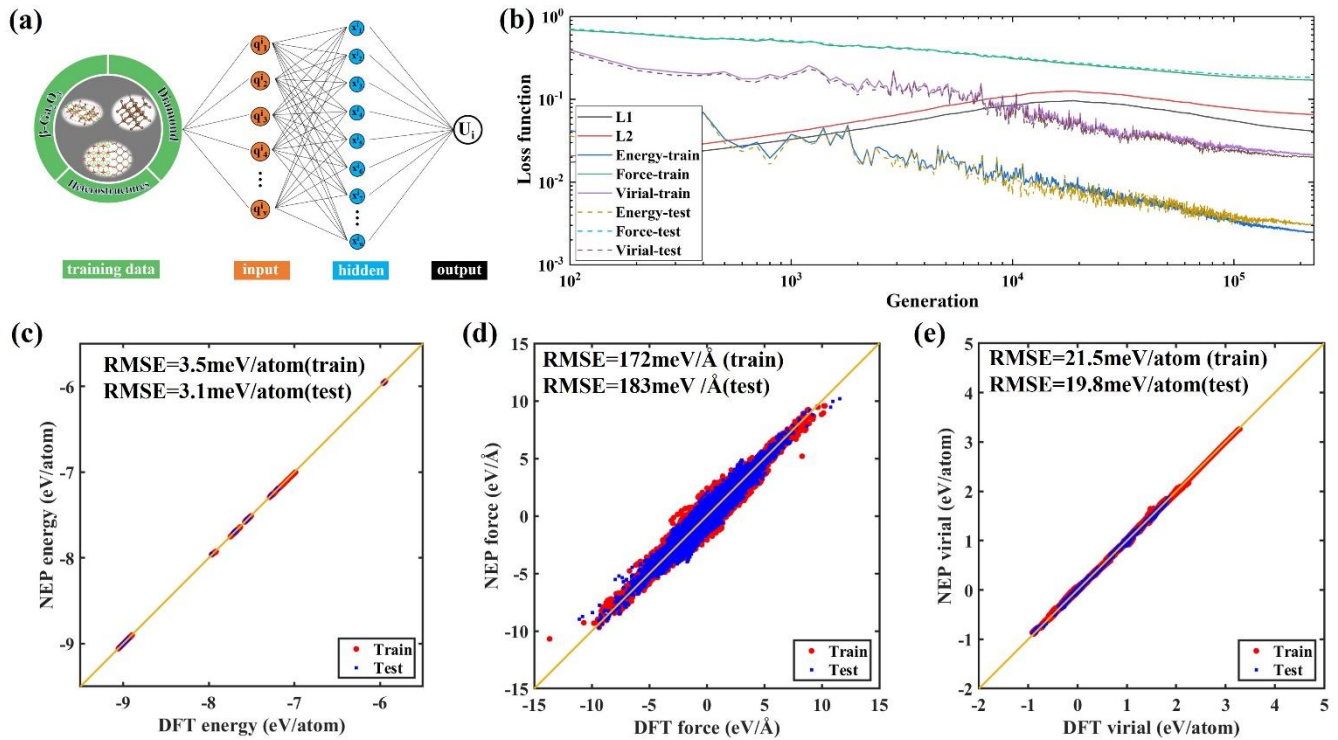


Figure 1. (a) Simplified schematic representation of the NEP framework. (b) Evolution of loss functions during the training process. L1 and L2 are regularizations. (c)–(e) Comparison between the NEP predictions and DFT reference values of energy, force, and virial for the training and test sets.

2.2 Details of training data and mechanical behavior

To investigate the heat transfer across the β -Ga₂O₃/diamond interface, a training dataset consisting of β -Ga₂O₃, diamond, and their heterostructures was constructed. The interfacial bonding of β -Ga₂O₃ and diamond for the β -Ga₂O₃/diamond heterostructure is relatively complex. In order to be more consistent with the situation in the experiment, the (100), (010) and (001) planes of β -Ga₂O₃ and the (100), (111) planes of diamond were mainly considered. At the same time, the O-C or Ga-C bonding at the β -Ga₂O₃/diamond initial interface was also considered. Hence, there were 10 types of heterostructures in the training data. *Ab initio* MD simulations were used to obtain the MD trajectories using the Vienna *Ab Initio* Simulation Package (VASP).^{39, 40} Finally, 1200, 1200, and 9000 *ab initio* configurations were obtained for pristine β -Ga₂O₃, pristine diamond, and their heterostructures, respectively, among which 2/3 were included in the training dataset and 1/3 were included in the test dataset. It was worth noting that the element diffusion phenomenon at the ideal interface of the heterogeneous structures was not considered in this work, which might occur at the β -Ga₂O₃/diamond interface and was important for the practical applications of the heterogeneous structures.^{41, 42}

The loss terms for energy, force, and virial relations in the test and training datasets showed very good

convergence after 230000 generations as depicted in Fig. 1(b). Parity plots of the energies, atomic forces, and atomic virial relations predicted from the NEP and DFT are shown in Fig. 1(c–e), showing good correlations. The root-mean-squared error (RMSE) of the predictions has also been presented. Generally, the RMSE values of each trained MLP model fell in the range of several meV/atom in terms of energy and several hundred meV/Å in terms of force, indicating satisfactory training.⁴³ The bond lengths of different bonds in the system were predicted using DFT and NEP method. As shown in Table 1, the bond lengths predicted by DFT and NEP were in good agreement, further confirming the good performance of the training. The training hyperparameters have been shown in Table 2. Further verification of the NEP accuracy for the interfacial bond formation including the comparison of the binding energies, the energies of the heterostructures at different interfacial distances and the energy differences before and after relaxation at different heterogeneous interfaces predicted from the NEP and DFT calculations can be found in the supporting information.

Table 1. The bond lengths predicted by DFT and NEP.

	C-C	C-Ga	C-O	Ga-O
DFT	1.55 Å	2.03 Å	1.43 Å	1.93 Å
NEP	1.53 Å	2.01 Å	1.39 Å	1.89 Å

Table2. NEP training hyperparameters.

Parameter	Value	Parameter	Value
r_C^R	8 Å	r_C^A	4 Å
n_{max}^R	8	n_{max}^A	8
N_{basis}^R	8	N_{basis}^A	8
l_{max}^{3b}	4	l_{max}^{4b}	2
type	3 Ga O C	λ_1	0.05
λ_2	0.05	λ_e	1.0
λ_f	1.0	λ_v	0.1
N_{neuron}	60	N_{batch}	2300
$N_{population}$	50	$N_{generation}$	230000

2.3 Equilibrium molecular dynamics (EMD) method and models

Based on the Green-Kubo approach, EMD simulations were utilized to assess the thermal conductivity⁴⁴⁻⁴⁶. The Green-Kubo formula connects fluctuations in heat current to thermal conductivity through the use of the autocorrelation function, as follows⁴⁷:

$$k_\alpha(t) = \frac{1}{k_B T^2 V} \int_0^{t_0} \langle J_\alpha(0) J_\alpha(t) \rangle dt \quad (2)$$

where k_α represents the thermal conductivity in the α direction, k_B is the Boltzmann constant, V is the volume of the model cell, T is the temperature, t_0 is the integral upper limit (which should theoretically be infinite), J_α is the component of heat current J in the α direction, and $\langle J_\alpha(0) J_\alpha(t) \rangle$ represents the ensemble average.

As shown in Fig. 2, β -Ga₂O₃ has a $C2/m$ crystal symmetry,⁴⁸ and each conventional unit cell includes 8 gallium atoms and 12 oxygen atoms. Diamond has an $Fd-3m$ crystal symmetry, and each conventional unit cell contains 8 carbon atoms. In EMD simulation, the bulk of the β -Ga₂O₃ system, consisting of $4 \times 15 \times 8$ conventional unit cells, includes 9600 atoms, and the bulk of the diamond system, consisting of $10 \times 10 \times 10$ conventional unit cells, includes 8000 atoms. In this work, cell structures were visualized using VESTA software.⁴⁹ The model in this study was more than 130% larger than that in similar previous work.^{11, 25, 50} Furthermore, the convergence tests on the model size were conducted, and the detailed information could be found in the supporting information. As a result, it could be shown that the size convergence was very good for the diamond and β -Ga₂O₃ model. Periodic boundary conditions were applied in all three directions. To reduce calculation errors, 50 independent MD runs were performed to obtain the average κ values with time steps of 1 fs at 200, 300, 400, 500, and 600 K.

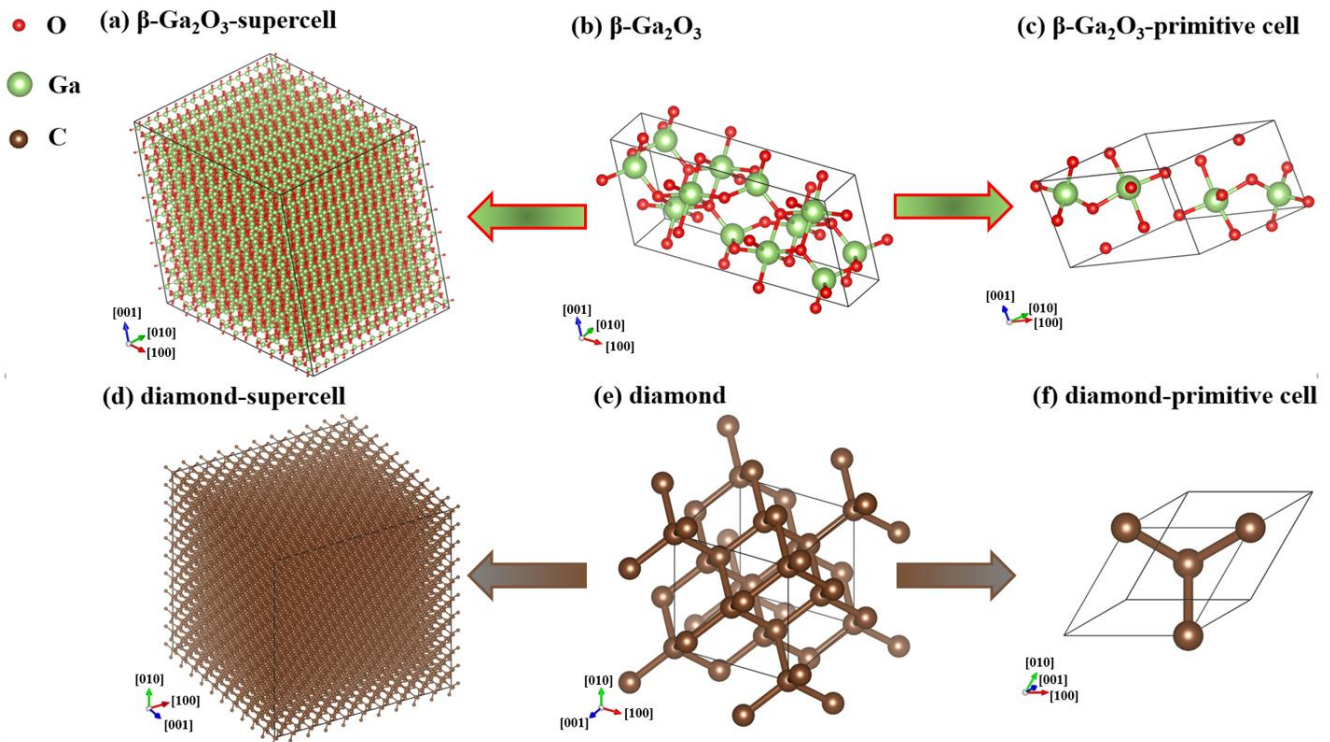


Figure 2. Supercell of (a) β -Ga₂O₃ and (d) diamond crystals, the conventional unit cell of (b) β -Ga₂O₃ and (e) diamond crystals, and primitive cell of (c) β -Ga₂O₃ and (f) diamond crystals.

2.4 Non-equilibrium molecular dynamics (NEMD) method and models

The NEMD method follows Fourier's law and divides the system into three distinct parts: a heat source that continuously supplies energy to the system, a heat sink that continuously releases energy from the system, and an effective part for measuring thermal conductivity. The law of energy conservation must be strictly observed during the NEMD simulation process. If the interatomic potential is not sufficiently accurate, it will be difficult to maintain consistent energy flow out of the heat source and into the heat sink. Therefore, NEMD

simulations could be considered as a measure of stability for NEP. If the accuracy of the NEP is insufficient, the system will collapse during the NEMD simulation.⁵¹ Figure 3(b) shows that the energy values of the heat source flowing into the system and the heat sink flowing out of the system are highly symmetrical about $E = 0$, which satisfies the law of energy conservation. It could also be confirmed that the accuracy of our NEP was sufficient. The heat flux J_Q generated in the NEMD process can be defined as:

$$J_Q = \frac{|dQ/dt|}{A} \quad (3)$$

where A and $|dQ/dt|$ represent the area of the simulation box perpendicular to the heat fluent and the energy exchange rate, respectively. To reduce the impact of interface area division, the interface area of the model was set to a uniform size. The temperature difference ΔT was obtained from the temperature distribution in the abovementioned interface region. The thermal boundary resistance (TBR) could be considered analogous to the thermal conductivity and be calculated as the formula⁵²:

$$\text{TBR} = \frac{\Delta T}{J_Q} \quad (4)$$

A time step of 0.5 fs was chosen. The 0.1 ns heat bath was first used to stabilize the system temperature at 300 K, and the 0.5 ns equilibration was then performed to stabilize the heat flow with the Langevin thermostat. Finally, the temperature profile was obtained by running the system for 2 ns. The relevant data were sampled after every 1000 time steps and averaged after every 50 data points before being recorded. The above process was repeated 80 times, and the final temperature profile was obtained after averaging. Considering the actual situation in industrial applications, a heat source ($T_{\text{source}} = 325$ K) and heat sink ($T_{\text{sink}} = 275$ K) were placed at the end of β -Ga₂O₃ and diamond, respectively, and the heat flow was from β -Ga₂O₃ to diamond. During the simulation, the outermost layers of about 3 Å in the z direction on each side were fixed to maintain close contact with each other. The middle part of the model used for heat transfer was divided into about 60 slices along the z direction. The thickness of each slice was about 5 Å. The temperature of each slice was calculated to obtain the temperature profile. Periodic boundary conditions were used in the x and y directions. The model size exceeded $5 \times 5 \times 30$ nm³, including more than 100000 atoms (varying slightly depending on the crystal orientation), as shown in Fig. 3(a). In the heterogeneous structures composed of different crystal orientations, the mismatch between β -Ga₂O₃ and diamond in the x - y plane were all less than 1.5%. The equilibrium lattice constants of β -Ga₂O₃ and diamond as well as the detailed information for their lattice mismatch could be found in the supporting information. Furthermore, the interface structures within the heterogeneous system could be proven to be of a high level of stability throughout the relaxation and NEMD simulation processes, as all the simulations could be successfully completed.

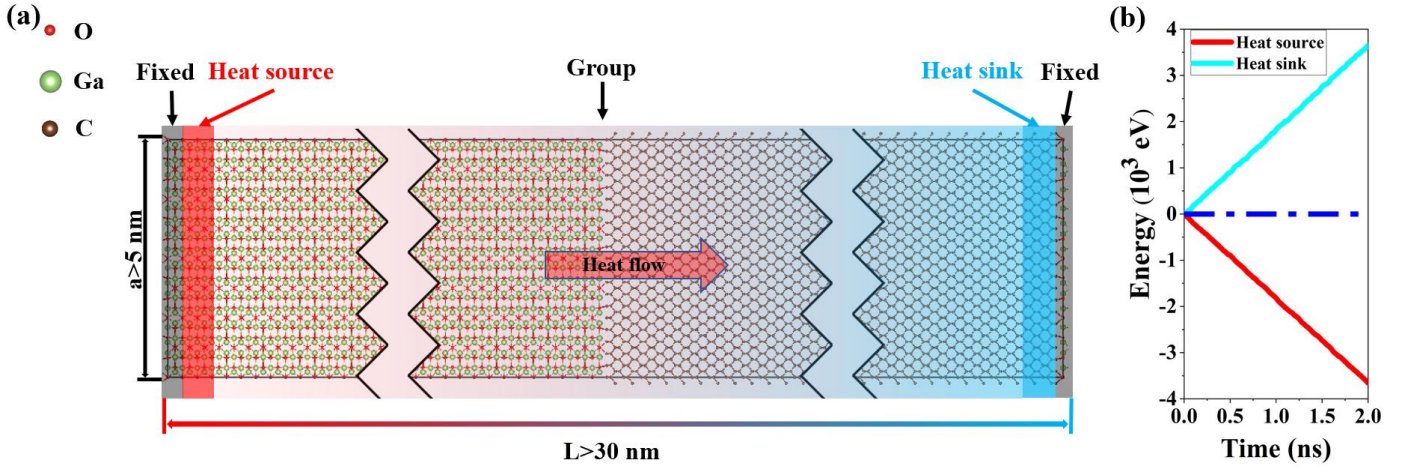


Figure 3. (a) Schematic diagram of NEMD simulation. (b) The cumulative energy of the heat source domain and heat sink domain varying as a function of the simulation time.

3. Results and discussion

3.1 Bulk thermal properties

The bulk thermal properties of β -Ga₂O₃ and diamond were predicted for verifying the accuracy of the trained NEP, which was proven to be sufficiently high for the prediction of the interfacial heat transfer properties of the β -Ga₂O₃/diamond heterostructure. The phonon dispersion is regarded as one of the most important thermal properties, which is also commonly used for the evaluation of the interatomic potentials. As shown in Fig. 4(a, b), the phonon dispersion of β -Ga₂O₃ and diamond calculated by NEP were in good agreement with the results calculated using the DFT (density functional theory) method. In this work, the primitive cell of the crystal was used to calculate the phonon dispersion as depicted in Fig. 2(c, f). The NEP was shown to enable accurate prediction for the thermal properties of β -Ga₂O₃ and diamond. Considering the low symmetry and high anisotropy of β -Ga₂O₃, it is reasonable and reliable that the phonon dispersion of β -Ga₂O₃ was more complex than that of diamond.^{6, 53} At 200–600 K, the thermal conductivity values of diamond and β -Ga₂O₃ predicted by NEP exhibited excellent agreement with the reported experimental and computational values, as depicted in Fig. 4(c, d) The above observations could show that our NEP could accurately predict the thermal properties of β -Ga₂O₃ and diamond, which could thus be used to investigate the interfacial heat transfer properties of the β -Ga₂O₃/diamond heterostructure.

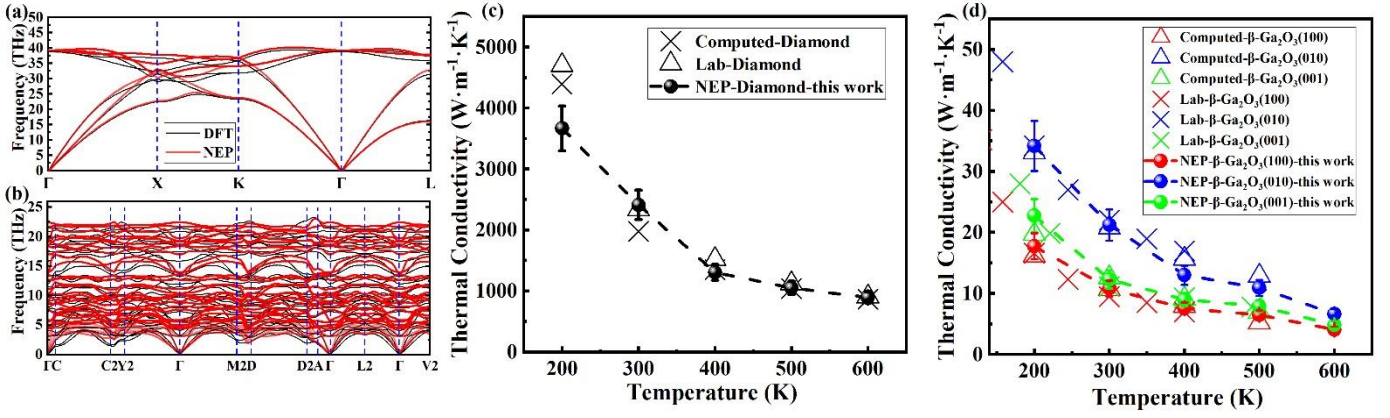


Figure 4. Phonon dispersion of (a) diamond, and (b) β -Ga₂O₃. (c) Temperature-dependent thermal conductivity calculated from NEP-EMD of diamond (solid circles) compared with the reported experimental values¹² (solid crosses) and computational values¹³ (hollow triangles). (d) Temperature-dependent thermal conductivity calculated from NEP-EMD for different crystal orientations of β -Ga₂O₃ (solid circles) compared with the reported experimental values⁵⁴ (solid crosses) and computational values²⁵ (hollow triangles). Each of the thermal conductivity values is the average of 50 independent simulations.

3.2 Heat transfer of β -Ga₂O₃/diamond interfaces

The interfacial heat transfer of β -Ga₂O₃/diamond heterostructures was further studied through NEMD simulations based on NEP. The stable temperature distribution of the β -Ga₂O₃/diamond heterostructures composed of different interfaces between β -Ga₂O₃ and diamond could be shown in Fig. 5(a–j). There was an obvious temperature jump (ΔT) at the β -Ga₂O₃/diamond interface, implying a finite TBR between β -Ga₂O₃ and diamond. The experimentally measured thermal boundary conductance (TBC) of the β -Ga₂O₃/diamond heterostructure by interfacial bonding was about 179 MW·m⁻²·K⁻¹ (TBR: 5.6 m²·K·GW⁻¹),²⁰ which agreed very well with the predicted TBR values in the range of 2.5 to 4.5 m²·K·GW⁻¹ in this work. It could be found that our calculated TBR was an order of magnitude lower than the that of the β -Ga₂O₃/diamond heterostructure by van der Waals interactions,^{16, 27} which was also similar to the reported experimental results by Graham et al.²⁰ This was because the bonding force for the interface bonding was much larger than the van der Waals force. In the β -Ga₂O₃/diamond heterostructure, the heat transfer primarily relied on lattice vibrations, and the strength of interface bonding was crucial for the efficiency of lattice vibration transmission at the interface. If the interface bonding was too weak, it would be very difficult to transmit the lattice vibrations. Therefore, to some extent, strengthening the interface bonding could be beneficial for the transmission of lattice vibrations, eventually reducing the thermal boundary resistance. By exploring the influence of the crystal orientations of β -Ga₂O₃, it could be found that $1/\text{TBR}_{\beta\text{-Ga}_2\text{O}_3(010)} > 1/\text{TBR}_{\beta\text{-Ga}_2\text{O}_3(001)} > 1/\text{TBR}_{\beta\text{-Ga}_2\text{O}_3(100)}$, which was consistent with $\kappa_{\beta\text{-Ga}_2\text{O}_3(010)} > \kappa_{\beta\text{-Ga}_2\text{O}_3(001)} > \kappa_{\beta\text{-Ga}_2\text{O}_3(100)}$. It could be indicated that the trend of $1/\text{TBR}$ for the β -Ga₂O₃/diamond heterostructure was highly similar to that of thermal conductivity for the corresponding crystal orientations of β -Ga₂O₃. As shown in Fig. 6(a, b), the VDOS for different crystal orientations of diamond

varied in a similar fashion and showed nearly no significant difference, while for $\beta\text{-Ga}_2\text{O}_3$, distinct differences in VDOS could be observed among different crystal orientations. It was probably one of the main reasons why the trend of $1/\text{TBR}$ aligned with the trend of thermal conductivity of different crystal orientations of $\beta\text{-Ga}_2\text{O}_3$. Furthermore, the thermal conductivity value of diamond (111) was approximately 80% of the thermal conductivity value of diamond (100). The thermal conductivity values of $\beta\text{-Ga}_2\text{O}_3$ (100) and $\beta\text{-Ga}_2\text{O}_3$ (001) were approximately 45% and 55% of the thermal conductivity of $\beta\text{-Ga}_2\text{O}_3$ (010), respectively. Therefore, compared to the differences in thermal conductivity values of various crystal orientations of $\beta\text{-Ga}_2\text{O}_3$, the differences in thermal conductivity values between diamond (100) and diamond (111) were not very obvious. From Equation (4), it could be observed that the change in temperature ΔT could have a significant impact on the TBR when the J_Q was constant. One of the main factors influencing ΔT was the thermal conductivity of the materials in the heterogeneous structure. Therefore, compared to diamond, the changes of thermal conductivity would be more obvious when the crystal orientation of $\beta\text{-Ga}_2\text{O}_3$ varied, leading to a noticeable change in ΔT , which in turn affected the TBR. It was probably another main reason why the trend of $1/\text{TBR}$ aligned with the trend of the corresponding crystal orientations of $\beta\text{-Ga}_2\text{O}_3$. The (010) crystal orientation of $\beta\text{-Ga}_2\text{O}_3$ was the best choice for integration with diamond when considering the interfacial heat transfer. Actually, the (100) and (001) planes of $\beta\text{-Ga}_2\text{O}_3$ were also widely used in $\beta\text{-Ga}_2\text{O}_3$ -based devices.⁵⁵⁻⁵⁸ Therefore, it was also very meaningful to explore the interfacial heat transfer of heterostructures composed of $\beta\text{-Ga}_2\text{O}_3$ (100/001) and diamond. From the perspective of the interfacial heat transfer efficiency of the heterostructure, $\beta\text{-Ga}_2\text{O}_3$ (001) was the alternative option, followed by $\beta\text{-Ga}_2\text{O}_3$ (100).

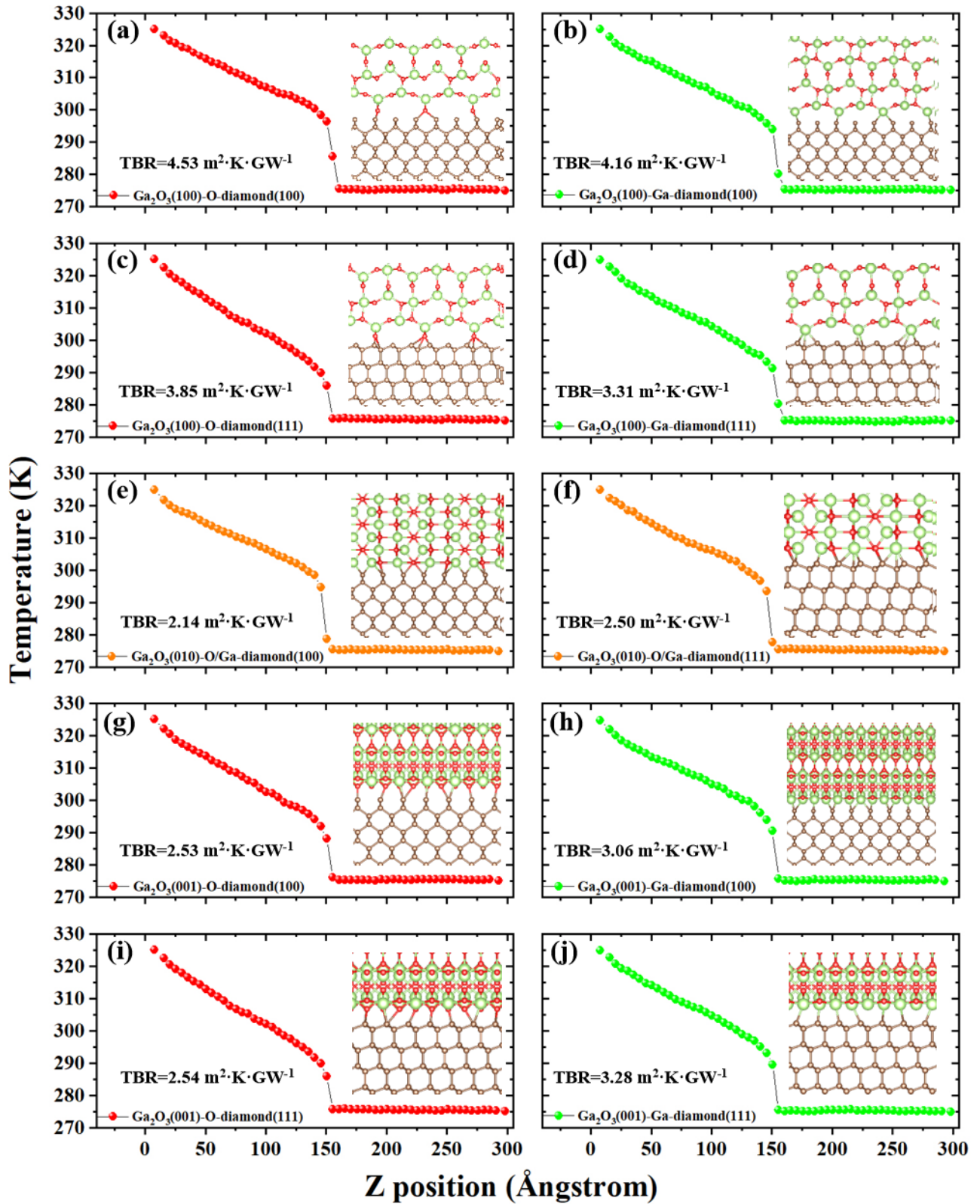


Figure 5. Corresponding temperature profiles of (a) β - $\text{Ga}_2\text{O}_3(100)$ -O-diamond(100), (b) β - $\text{Ga}_2\text{O}_3(100)$ -Ga-diamond(100), (c) β - $\text{Ga}_2\text{O}_3(100)$ -O-diamond(111), (d) β - $\text{Ga}_2\text{O}_3(100)$ -Ga-diamond(111), (e) β - $\text{Ga}_2\text{O}_3(010)$ -O/Ga-diamond(100), (f) β - $\text{Ga}_2\text{O}_3(010)$ -O/Ga-diamond(111), (g) β - $\text{Ga}_2\text{O}_3(001)$ -O-diamond(100), (h) β - $\text{Ga}_2\text{O}_3(001)$ -Ga-diamond(100), (i) β - $\text{Ga}_2\text{O}_3(001)$ -O-diamond(111), and (j) β - $\text{Ga}_2\text{O}_3(001)$ -Ga-diamond(111). The bonding at the interface in the figure is in the state before relaxation. Only the structure of the initial state is shown.

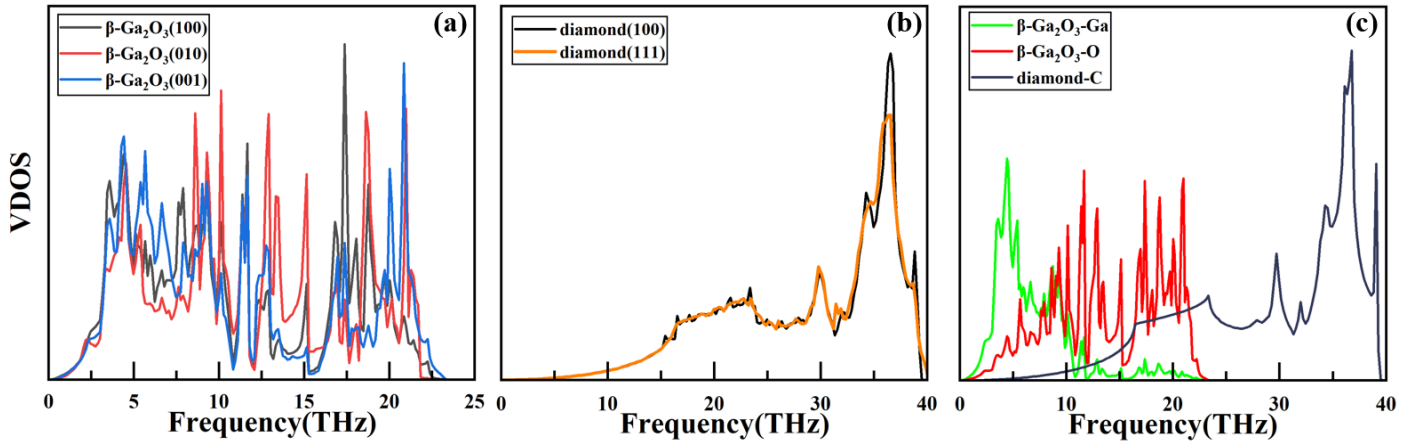


Figure 6. The vibration density of states (VDOS) of (a) β -Ga₂O₃ (100/010/001), (b) diamond (100/111), and (c) β -Ga₂O₃-Ga/O and diamond-C.

The differences in TBR were discussed based on the crystal orientations of diamond. It could be found that $TBR_{\text{diamond}(111)} < TBR_{\text{diamond}(100)}$ when diamond was integrated with β -Ga₂O₃ (100), and $TBR_{\text{diamond}(100)} < TBR_{\text{diamond}(111)}$ when diamond was integrated with β -Ga₂O₃ (010) and β -Ga₂O₃ (001). The above phenomena were complicated, so that the distribution of thermal conductivity vs phonon frequency was calculated, as depicted in Fig. 7(a, b). To better present the frequency range of high thermal conductivity contributions of β -Ga₂O₃, the part of thermal conductivity spectra greater than 15% of the peak value was defined as the effective part. The black, red, and blue dashed lines in Fig. 7(a) were the dividing lines of the effective parts of β -Ga₂O₃ (100), (010), and (001), respectively. The part of thermal conductivity spectra above the dividing line was the effective part. The effective cutoff frequency of the phonon contribution to the thermal conductivity was thus obtained, which was defined as the effective part cutoff frequency (EPCF). The black, red, and blue dotted lines in Fig. 7(a) were the EPCF of β -Ga₂O₃ (100), (010), and (001), respectively. To facilitate a better comparison of the high thermal conductivity contribution frequency for β -Ga₂O₃ and diamond, the EPCFs of the three crystal orientations of β -Ga₂O₃ were also plotted in the thermal conductivity spectra of diamond (100) and (111) using the auxiliary lines. The horizontal coordinate axis (Frequency) of the thermal conductivity spectra for β -Ga₂O₃ and diamond were also aligned to make it easier for the comparison of the thermal conductivity spectra. The effective frequency portions of β -Ga₂O₃ (100), (010) and (001) were shaded in black, red, and blue, respectively. From Fig. 7(b), it could be clearly observed that the TBR of β -Ga₂O₃/diamond was mainly affected by low-frequency phonons of diamond. The main difference between the diamond (100) orientation and the diamond (111) orientation was the first peak of the thermal conductivity spectra. The first peak of diamond (100) is in the range of 2.5-5 THz, and that of the diamond (111) is in the range of 1.5-3.5 THz. The $EPCF_{\beta\text{-Ga}_2\text{O}_3(100)}$ mainly overlapped with the first peak of the diamond (111) and had little overlap with the first peak of diamond (100). This was why $TBR_{\text{diamond}(111)} < TBR_{\text{diamond}(100)}$ when diamond was integrated with β -Ga₂O₃ (100). In contrast, $EPCF_{\beta\text{-Ga}_2\text{O}_3(010)}$ and $EPCF_{\beta\text{-Ga}_2\text{O}_3(001)}$ were not only overlapped with the first peak of diamond (111) but also more coincident with the diamond (100) peak.

Therefore, $TBR_{\text{diamond}(100)} < TBR_{\text{diamond}(111)}$ when diamond integrated with $\beta\text{-Ga}_2\text{O}_3(010)$ and $\beta\text{-Ga}_2\text{O}_3(001)$. In general, the diamond (111) plane was the best when the diamond formed a heterostructure with $\beta\text{-Ga}_2\text{O}_3(100)$, and the diamond (100) plane was the best choice when the diamond formed a heterostructure with $\beta\text{-Ga}_2\text{O}_3(010)$ and $\beta\text{-Ga}_2\text{O}_3(001)$.

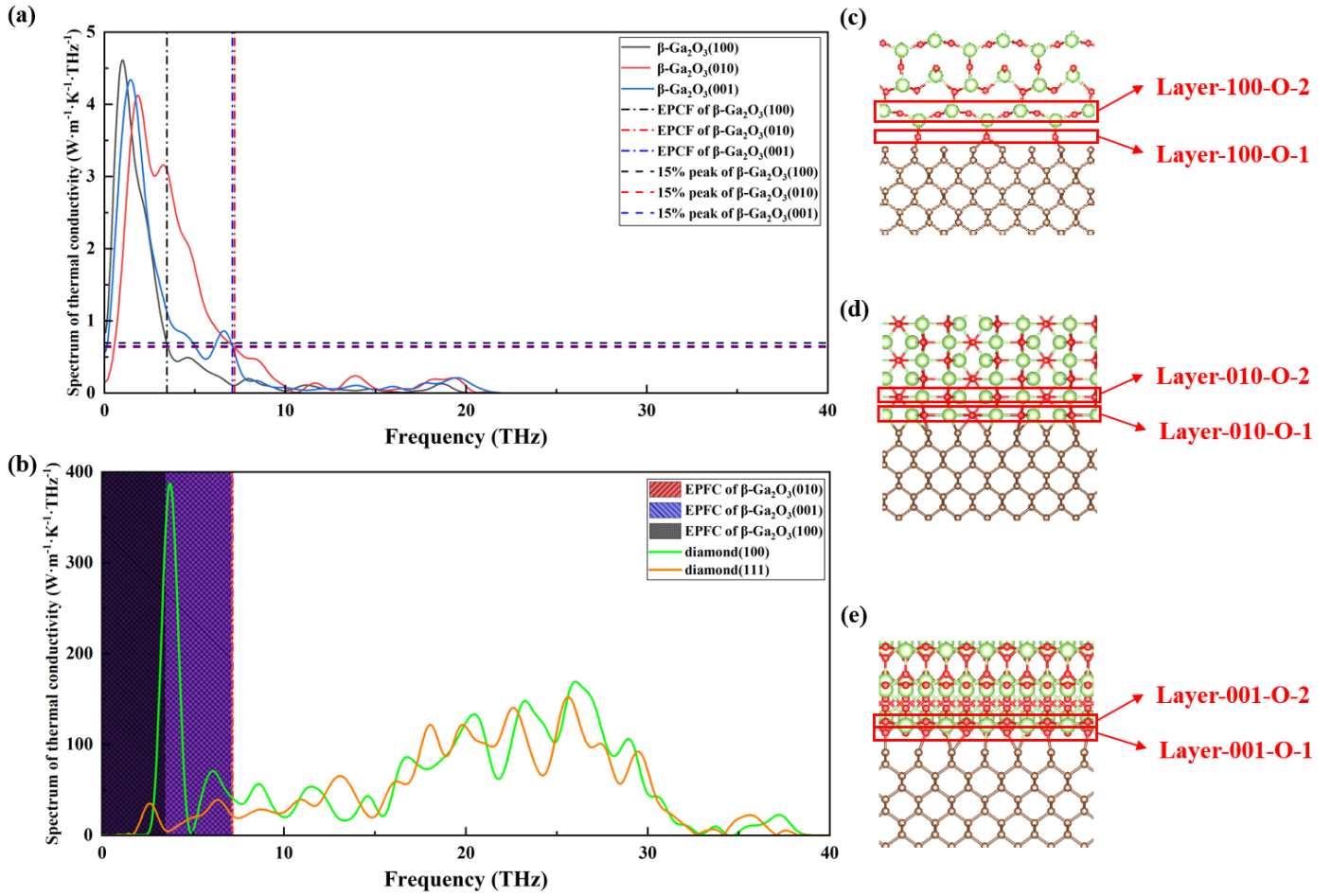


Figure 7. (a) Thermal conductivity spectra of $\beta\text{-Ga}_2\text{O}_3(100)$, $\beta\text{-Ga}_2\text{O}_3(010)$, and $\beta\text{-Ga}_2\text{O}_3(001)$. (b) Thermal conductivity spectra of diamond (100) and diamond (111). O atom grouping diagrams of (c) $\beta\text{-Ga}_2\text{O}_3(100)$, (d) $\beta\text{-Ga}_2\text{O}_3(001)$, and (e) $\beta\text{-Ga}_2\text{O}_3(001)$.

The effects of interfacial atoms and crystal orientations on the thermal conductivity of the $\beta\text{-Ga}_2\text{O}_3$ /diamond heterostructure have been investigated. For convenience, the O atoms in $\beta\text{-Ga}_2\text{O}_3$ were labeled by layer number, as shown in Fig. 7(c–e). It could be found that the TBR of $\beta\text{-Ga}_2\text{O}_3(100)$ was smaller in the case of initial Ga-C bonding than initial O-C bonding, while the TBR of $\beta\text{-Ga}_2\text{O}_3(001)$ was smaller in the case of initial O-C bonding than initial Ga-C bonding. Ga and O atoms in the $\beta\text{-Ga}_2\text{O}_3(010)$ plane were on the same horizontal plane, and Ga and O atoms were bonded to C atoms at the same time, as shown in Fig. 7(d). Thus, the $\beta\text{-Ga}_2\text{O}_3(010)$ was not discussed here. As shown in Table 1 and Table 3, in $\beta\text{-Ga}_2\text{O}_3(100/001)$ /diamond heterostructures, the nearest vertical distance between Ga atoms and C atoms as well as between O atoms and C atoms were both smaller than the corresponding bond lengths after relaxation. It could be implied that both Ga-C bonds and O-C bonds existed at the same time at the interface after relaxation. As shown in Fig. 8(a-h), the interface structures before and after relaxation were displayed. It could be observed

that whether the interface initially consisted of Ga-C bonds or O-C bonds, after relaxation, both Ga-C bonds and O-C bonds would coexist. In Fig. 6(c), it could be observed that the frequency range overlap between O atoms and C atoms was higher compared to that between Ga atoms and C atoms, implying that the O-C bonds were more beneficial to the heat transfer at the interface. Hence, it could be inferred that the quantity of O-C bonds at the interface could significantly influence the TBR.

Table 3. Nearest vertical distance (vertical distance is the distance between the planes of two atoms along the Z direction represented by \perp) between Ga/O and C atoms at the interface in the β -Ga₂O₃ (100/001)/diamond (111) before and after relaxation

	β -Ga ₂ O ₃ (100)-Ga-diamond (111)	β -Ga ₂ O ₃ (100)-Ga-diamond (111)
	before relaxation	after relaxation
Ga \perp C	1.10 Å	1.62 Å
O \perp C	2.01 Å	1.16 Å
	β -Ga ₂ O ₃ (001)-Ga-diamond (111)	β -Ga ₂ O ₃ (001)-Ga-diamond (111)
	before relaxation	after relaxation
Ga \perp C	1.10 Å	1.33 Å
O \perp C	1.40 Å	1.19 Å
	β -Ga ₂ O ₃ (100)-O-diamond (111)	β -Ga ₂ O ₃ (100)-O-diamond (111)
	before relaxation	after relaxation
Ga \perp C	2.16 Å	1.35 Å
O \perp C	1.10 Å	0.85 Å
	β -Ga ₂ O ₃ (001)-O-diamond (111)	β -Ga ₂ O ₃ (001)-O-diamond (111)
	before relaxation	after relaxation
Ga \perp C	1.64 Å	1.71 Å
O \perp C	1.10 Å	1.24 Å

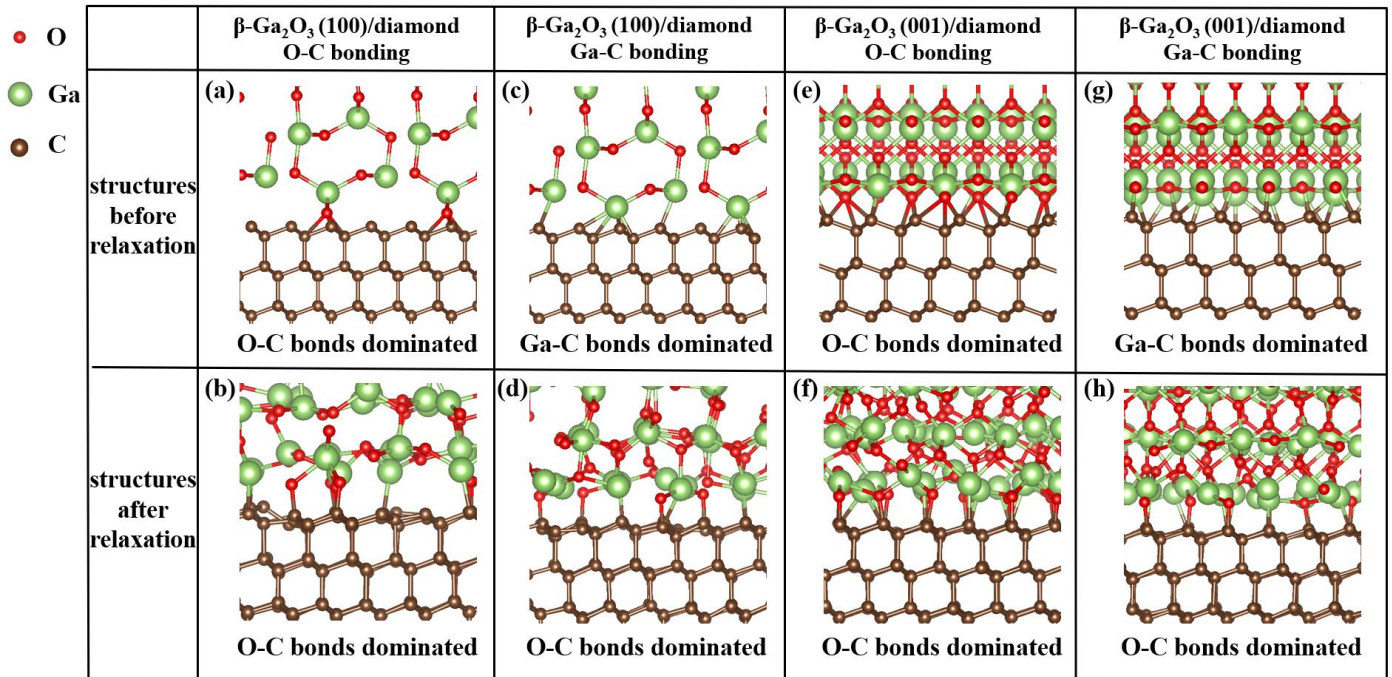


Figure 8. (a) β -Ga₂O₃ (100)-O-diamond before relaxation. (b) β -Ga₂O₃ (100)-O-diamond after relaxation. (c) β -Ga₂O₃ (100)-Ga-diamond before relaxation. (d) β -Ga₂O₃ (100)-Ga-diamond after relaxation. (e) β -Ga₂O₃ (001)-O-diamond before relaxation. (f) β -Ga₂O₃ (001)-O-diamond after relaxation. (g) β -Ga₂O₃ (001)-Ga-diamond before relaxation. (h) β -Ga₂O₃ (001)-Ga-diamond after relaxation.

As shown in Fig. 7(c), the number of O atoms in Layer-100-O-1 was smaller than in Layer-100-O-2. When the O atoms of β -Ga₂O₃ (100) bonded to the C atoms of diamond at the initial interface, the C atoms bonded to Layer-100-O-1 after relaxation, as depicted in Fig. 8(a, b). When the Ga atoms of β -Ga₂O₃ (100) bonded to the C atoms of diamond at the initial interface, the C atoms bonded to Layer-100-O-2 after relaxation, as depicted in Fig. 8(c, d). This caused the number of bonds formed when O-C bonding at the initial interface to be less than that formed when Ga-C bonding at the initial interface in the β -Ga₂O₃ (100) crystal orientation, which could explain the reason for $TBR_{\beta\text{-Ga}_2\text{O}_3(100)\text{-O-diamond}} > TBR_{\beta\text{-Ga}_2\text{O}_3(100)\text{-Ga-diamond}}$. For the same reason, $TBR_{\beta\text{-Ga}_2\text{O}_3(001)\text{-O-diamond}} < TBR_{\beta\text{-Ga}_2\text{O}_3(001)\text{-Ga-diamond}}$ was also caused by the number of bonds between O and C atoms. As depicted in Fig. 7(e), The difference was that Layer-001-O-1 and Layer-001-O-2 in the β -Ga₂O₃ (001) crystal orientation were very close. Therefore, with O-C bonding at the initial interface in the β -Ga₂O₃ (001) crystal orientation, Layer-001-O-1 and Layer-001-O-2 were bonded to C atoms at the same time after relaxation, as depicted in Fig. 8(e, f). In contrast, when Ga-C bonding at the initial interface in the β -Ga₂O₃ (001) crystal orientation, only Layer-001-O-2 bonded to C atoms after relaxation, as depicted in Fig. 8(g, h). Therefore, the number of bonds formed after relaxation when O-C bonding at the initial interface was greater than that formed when Ga-C bonding at the initial interface in the β -Ga₂O₃(001) crystal orientation, which was the reason for $TBR_{\beta\text{-Ga}_2\text{O}_3(001)\text{-O-diamond}} < TBR_{\beta\text{-Ga}_2\text{O}_3(001)\text{-Ga-diamond}}$. In general, the Ga-C bonding at the initial interface was best when the diamond formed a heterostructure with β -Ga₂O₃ (100). When the diamond formed a heterostructure with β -Ga₂O₃ (001), O-C bonding at the initial interface was the best choice.

4. Conclusion

An NEP for the prediction of the interfacial thermal transfer properties was trained via GPUMD based on the machine learning method. The phonon dispersion and thermal conductivity of diamond and β -Ga₂O₃ at different temperatures were predicted using this NEP. The phonon dispersion predicted by NEP agreed well with that calculated by DFT. At the same time, the thermal conductivity at different temperatures predicted by NEP was in great agreement with the values previously reported by other groups. Thus, it could be confirmed that our NEP had high accuracy and could be used to predict the interfacial heat transfer of β -Ga₂O₃/diamond heterostructures, which was then explored using the NEMD method. Finally, the TBR of heterostructures composed of β -Ga₂O₃ and diamond with different crystal orientations has been predicted, and the accuracy of our predictions was demonstrated by the comparison with the experimental values from other groups.

On this basis, the TBR of the β -Ga₂O₃/diamond interfaces were predicted. In order to explore the reasons for the difference of TBR at different interfaces, the effects of crystal orientations and interfacial atoms on the

TBR of β -Ga₂O₃/diamond interfaces were studied from the perspectives of thermal conductivity value, thermal conductivity spectra, vibration density of states and interfacial structures. The heterostructure with the smallest TBR ($\sim 2.14 \text{ m}^2 \cdot \text{K} \cdot \text{GW}^{-1}$) among all interfaces is β -Ga₂O₃ (010)/diamond (100). In the end, to provide detailed guidance on the selection of crystal orientations and interfacial atoms for the β -Ga₂O₃/diamond heterostructure, the optimization strategies were proposed as follows:

(1) When selecting the crystal orientation of β -Ga₂O₃ for the β -Ga₂O₃/diamond heterostructure, the (010) crystal plane should be the first choice, followed by the (001) crystal plane and finally the (100) crystal plane.

(2) It could be seen that β -Ga₂O₃ (100) is best paired with diamond (111), and in contrast, β -Ga₂O₃ (010) and β -Ga₂O₃ (001) are best paired with diamond (100).

(3) When β -Ga₂O₃ (100) is integrated with diamond, the initial interface bonded by Ga and C atoms is the best choice. When β -Ga₂O₃ (001) is integrated with diamond, the initial interface bonded by O and C atoms is the best choice.

Supporting Information

The performance of the NEP for interfacial bond formation; the size convergence test of diamond and β -Ga₂O₃; details of the model in the NEMD simulations.

Declaration of Competing Interest

The authors declare no conflict of interest.

Data Availability

The data that support the findings of this study are available from the corresponding author upon reasonable request. The potential files and reference dataset have been uploaded to the GitHub repository and are publicly available at <https://github.com/doulala333/Potential>.

Acknowledgements

This work was funded by the National Natural Science Foundation of China (Grant Nos. 52202045,

62004141), the Knowledge Innovation Program of Wuhan-Shuguang (Grant Nos. 2023010201020243, 2023010201020255), the Major Program (JD) of Hubei Province (Grant No. 2023BAA009), the Fundamental Research Funds for the Central Universities (Grant Nos. 2042023kf0112, 2042022kf1028), the Hubei Natural Science Foundation (Grant No. 2022CFB606), the Open Fund of Hubei Key Laboratory of Electronic Manufacturing and Packaging Integration (Grant Nos. EMPI2024014, EMPI2024021, EMPI2023027), and the China Scholarship Council (Grant No. 202206275005).

References

- (1) S. Pearton, J. Yang, P.H. Cary, F. Ren, J. Kim, M.J. Tadjer, M.A. Mastro, A review of Ga₂O₃ materials, processing, and devices. *Applied Physics Reviews* **2018**, 5, 011301.
- (2) T. Matsumoto, M. Aoki, A. Kinoshita, T. Aono, Absorption and reflection of vapor grown single crystal platelets of β-Ga₂O₃. *Japanese Journal of Applied Physics* **1974**, 13, 1578.
- (3) J. Zhang, P. Dong, K. Dang, Y. Zhang, Q. Yan, H. Xiang, J. Su, Z. Liu, M. Si, J. Gao, Ultra-wide bandgap semiconductor Ga₂O₃ power diodes. *Nature Communications* **2022**, 13, 3900.
- (4) C. Wang, J. Zhang, S. Xu, C. Zhang, Q. Feng, Y. Zhang, J. Ning, S. Zhao, H. Zhou, Y. Hao, Progress in state-of-the-art technologies of Ga₂O₃ devices. *Journal of Physics D: Applied Physics* **2021**, 54, 243001.
- (5) Z. Guo, A. Verma, X. Wu, F. Sun, A. Hickman, T. Masui, A. Kuramata, M. Higashiwaki, D. Jena, T. Luo, Anisotropic thermal conductivity in single crystal β-gallium oxide. *Applied Physics Letters* **2015**, 106, 111909.
- (6) Z. Sun, Z. Qi, K. Liang, X. Sun, Z. Zhang, L. Li, Q. Wang, G. Zhang, G. Wu, W. Shen, A neuroevolution potential for predicting the thermal conductivity of α, β, and ε-Ga₂O₃. *Applied Physics Letters* **2023**, 123, 192202.
- (7) J.S. Kang, M. Li, H. Wu, H. Nguyen, T. Aoki, Y. Hu, Integration of boron arsenide cooling substrates into gallium nitride devices. *Nature Electronics* **2021**, 4, 416-423.
- (8) Y. Cui, M. Li, Y. Hu, Emerging interface materials for electronics thermal management: experiments, modeling, and new opportunities. *Journal of Materials Chemistry C* **2020**, 8, 10568-10586.
- (9) Y. Cui, Z. Qin, H. Wu, M. Li, Y. Hu, Flexible thermal interface based on self-assembled boron arsenide for high-performance thermal management. *Nature Communications* **2021**, 12, 1284.
- (10) J.S. Kang, H. Wu, Y. Hu, Thermal properties and phonon spectral characterization of synthetic boron phosphide for high thermal conductivity applications. *Nano Letter* **2017**, 17, 7507-7514.
- (11) J. Xiong, Z. Qi, K. Liang, X. Sun, Z. Sun, Q. Wang, L. Chen, G. Wu, W. Shen, Molecular dynamics insights on thermal conductivities of cubic diamond, lonsdaleite and nanotwinned diamond via the machine learned potential. *Chinese Physics B* **2023**, 32, 680-687.
- (12) D. Onn, A. Witek, Y. Qiu, T. Anthony, W. Banholzer, Some aspects of the thermal conductivity of isotopically enriched diamond single crystals. *Physical Review Letters* **1992**, 68, 2806.
- (13) A. Ward, D. Broido, D.A. Stewart, G. Deinzer, Ab initio theory of the lattice thermal conductivity in diamond. *Physical Review B* **2009**, 80, 125203.
- (14) S. Li, Q. Zheng, Y. Lv, X. Liu, X. Wang, P.Y. Huang, D.G. Cahill, B. Lv, High thermal conductivity in cubic boron arsenide crystals. *Science* **2018**, 361, 579-581.
- (15) H. Kim, S. Tarelkin, A. Polyakov, S. Troschiev, S. Nosukhin, M. Kuznetsov, J. Kim, Ultrawide-bandgap pn heterojunction of diamond/β-Ga₂O₃ for a solar-blind photodiode. *ECS Journal of Solid State Science and Technology* **2020**, 9, 045004.
- (16) Z. Cheng, L. Yates, J. Shi, M.J. Tadjer, K.D. Hobart, S. Graham, Thermal conductance across β-Ga₂O₃-diamond van der Waals heterogeneous interfaces. *APL Materials* **2019**, 7, 031118.
- (17) T. Matsumae, Y. Kurashima, H. Umezawa, K. Tanaka, T. Ito, H. Watanabe, H. Takagi, Low-temperature direct bonding of β-Ga₂O₃ and diamond substrates under atmospheric conditions. *Applied Physics Letters* **2020**, 116, 141602.
- (18) T. Matsumae, H. Umezawa, Y. Kurashima, H. Takagi, Low-Temperature Direct Bonding of Wide-Bandgap Semiconductor Substrates. *ECS Transactions* **2023**, 111, 53.
- (19) P. Sittimart, S. Ohmagari, T. Matsumae, H. Umezawa, T. Yoshitake, Diamond/β-Ga₂O₃ pn heterojunction diodes fabricated by low-temperature direct-bonding. *AIP Advances* **2021**, 11, 105114.
- (20) Z. Cheng, V.D. Wheeler, T. Bai, J. Shi, M.J. Tadjer, T. Feygelson, K.D. Hobart, M.S. Goorsky, S. Graham, Integration of polycrystalline Ga₂O₃ on diamond for thermal management. *Applied Physics Letters* **2020**, 116, 062105.
- (21) J. Oh, J. Ma, G. Yoo, Simulation study of reduced self-heating in β-Ga₂O₃ MOSFET on a nano-crystalline diamond substrate. *Results in Physics* **2019**, 13, 102151.
- (22) Z. Qi, W. Shen, R. Li, X. Sun, L. Li, Q. Wang, G. Wu, K. Liang, AlN/diamond interface nanoengineering for reducing thermal boundary resistance by molecular dynamics simulations. *Applied Surface Science* **2023**, 615, 156419.
- (23) K. Ren, X. Liu, S. Chen, Y. Cheng, W. Tang, G. Zhang, Remarkable reduction of interfacial thermal resistance in nanophononic heterostructures. *Advanced Functional Materials* **2020**, 30, 2004003.
- (24) M. Hu, X. Zhang, D. Poulidakos, C.P. Grigoropoulos, Large “near junction” thermal resistance reduction in electronics by

- interface nanoengineering. *International Journal of Heat and Mass Transfer* **2011**, 54, 5183-5191.
- (25) R. Li, Z. Liu, A. Rohskopf, K. Gordiz, A. Henry, E. Lee, T. Luo, A deep neural network interatomic potential for studying thermal conductivity of β -Ga₂O₃. *Applied Physics Letters* **2020**, 117, 152102.
- (26) S. Dong, B. Yang, Q. Xin, X. Lan, X. Wang, G. Xin, Interfacial thermal transport of graphene/ β -Ga₂O₃ heterojunctions: A molecular dynamics study with a self-consistent interatomic potential. *Physical Chemistry Chemical Physics* **2022**, 24, 12837-12848.
- (27) A. Petkov, A. Mishra, J.W. Pomeroy, M. Kuball, Molecular dynamics study of thermal transport across Ga₂O₃-diamond interfaces. *Applied Physics Letters* **2023**, 122, 031602.
- (28) X. Wan, W. Feng, Y. Wang, H. Wang, X. Zhang, C. Deng, N. Yang, Materials discovery and properties prediction in thermal transport via materials informatics: a mini review. *Nano Letter*. **2019**, 19, 3387-3395.
- (29) Y.-J. Wu, L. Fang, Y. Xu, Predicting interfacial thermal resistance by machine learning. *npj Computational Materials* **2019**, 5, 56.
- (30) B. Mortazavi, E.V. Podryabinkin, S. Roche, T. Rabczuk, X. Zhuang, A.V. Shapeev, Machine-learning interatomic potentials enable first-principles multiscale modeling of lattice thermal conductivity in graphene/borophene heterostructures. *Materials Horizons* **2020**, 7, 2359-2367.
- (31) S. Wyant, A. Rohskopf, A. Henry, Machine learned interatomic potentials for modeling interfacial heat transport in Ge/GaAs. *Computational Materials Science* **2021**, 200, 110836.
- (32) Z. Fan, T. Siro, A. Harju, Accelerated molecular dynamics force evaluation on graphics processing units for thermal conductivity calculations. *Computer Physics Communications* **2013**, 184, 1414-1425.
- (33) B. Mortazavi, Z. Fan, L.F.C. Pereira, A. Harju, T. Rabczuk, Amorphized graphene: a stiff material with low thermal conductivity. *Carbon* **2016**, 103, 318-326.
- (34) Z. Fan, W. Chen, V. Vierimaa, A. Harju, Efficient molecular dynamics simulations with many-body potentials on graphics processing units. *Computer Physics Communications* **2017**, 218, 10-16.
- (35) Z. Fan, Z. Zeng, C. Zhang, Y. Wang, K. Song, H. Dong, Y. Chen, T. Ala-Nissila, Neuroevolution machine learning potentials: Combining high accuracy and low cost in atomistic simulations and application to heat transport. *Physical Review B* **2021**, 104, 104309.
- (36) T. Schaul, T. Glasmachers, J. Schmidhuber, High dimensions and heavy tails for natural evolution strategies, *Proceedings of the 13th Annual Conference on Genetic and Evolutionary Computation* **2011**, 845-852.
- (37) Z. Fan, Improving the accuracy of the neuroevolution machine learning potential for multi-component systems. *Journal of Physics: Condensed Matter* **2022**, 34, 125902.
- (38) Z. Fan, Y. Wang, P. Ying, K. Song, J. Wang, Y. Wang, Z. Zeng, K. Xu, E. Lindgren, J.M. Rahm, GPUMD: A package for constructing accurate machine-learned potentials and performing highly efficient atomistic simulations. *The Journal of Chemical Physics* **2022**, 157, 114801.
- (39) G. Kresse, J. Furthmüller, Efficiency of ab-initio total energy calculations for metals and semiconductors using a plane-wave basis set. *Computational Materials Science* **1996**, 6, 15-50.
- (40) G. Kresse, D. Joubert, From ultrasoft pseudopotentials to the projector augmented-wave method. *Physical Review B* **1999**, 59, 1758.
- (41) I. Bello, Y. Chong, K. Leung, C. Chan, K. Ma, W. Zhang, S. Lee, A. Layyous, Cubic boron nitride films for industrial applications. *Diamond and Related Materials* **2005**, 14, 1784-1790.
- (42) X. Yang, M. Pristovsek, S. Nitta, Y. Liu, Y. Honda, Y. Koide, H. Kawarada, H. Amano, Epitaxial combination of two-dimensional hexagonal boron nitride with single-crystalline diamond substrate. *ACS Applied Materials & Interfaces* **2020**, 12, 46466-46475.
- (43) H. Yanxon, D. Zagaceta, B. Tang, D.S. Matteson, Q. Zhu, PyXtal_FF: a python library for automated force field generation. *Machine Learning: Science and Technology* **2020**, 2, 027001.
- (44) X. Yu, R. Li, T. Shiga, L. Feng, M. An, L. Zhang, J. Shiomi, N. Yang, Hybrid thermal transport characteristics of doped organic semiconductor poly (3, 4-ethylenedioxythiophene): tosylate. *The Journal of Physical Chemistry C* **2019**, 123, 26735-26741.
- (45) R. Kubo, M. Toda, N. Hashitsume, *Statistical Physics II: Nonequilibrium Statistical Mechanics*, Springer Science & Business Media, Berlin, 2012.
- (46) H. Meng, X. Yu, H. Feng, Z. Xue, N. Yang, Superior thermal conductivity of poly (ethylene oxide) for solid-state electrolytes: A molecular dynamics study. *International Journal of Heat and Mass Transfer* **2019**, 137, 1241-1246.
- (47) R. Kubo, Statistical-mechanical theory of irreversible processes. I. General theory and simple applications to magnetic and conduction problems. *Journal of the Physical Society of Japan* **1957**, 12, 570-586.
- (48) J. Åhman, G. Svensson, J. Albertsson, A reinvestigation of β -gallium oxide. *Acta Crystallographica Section C: Crystal Structure Communications* **1996**, 52, 1336-1338.
- (49) K. Momma, F. Izumi, VESTA 3 for three-dimensional visualization of crystal, volumetric and morphology data. *Journal of Applied Crystallography* **2011**, 44, 1272-1276.
- (50) Y.-B. Liu, J.-Y. Yang, G.-M. Xin, L.-H. Liu, G. Csányi, B.-Y. Cao, Machine learning interatomic potential developed for molecular simulations on thermal properties of β -Ga₂O₃. *The Journal of Chemical Physics* **2020**, 153, 144501.
- (51) W. Sha, X. Dai, S. Chen, B. Yin, F. Guo, Phonon thermal transport in two-dimensional PbTe monolayers via extensive molecular dynamics simulations with a neuroevolution potential. *Materials Today Physics* **2023**, 34, 101066.
- (52) E.T. Swartz, R.O. Pohl, Thermal boundary resistance. *Reviews of Modern Physics* **1989**, 61, 605.
- (53) J. Zhao, J. Byggmästar, H. He, K. Nordlund, F. Djurabekova, M. Hua, Complex Ga₂O₃ polymorphs explored by accurate and general-purpose machine-learning interatomic potentials. *npj Computational Materials* **2023**, 9, 159.

- (54) P. Jiang, X. Qian, X. Li, R. Yang, Three-dimensional anisotropic thermal conductivity tensor of single crystalline β -Ga₂O₃. *Applied Physics Letters* **2018**, 113, 232105.
- (55) Q. He, W. Mu, H. Dong, S. Long, Z. Jia, H. Lv, Q. Liu, M. Tang, X. Tao, M. Liu, Schottky barrier diode based on β -Ga₂O₃ (100) single crystal substrate and its temperature-dependent electrical characteristics. *Applied Physics Letters* **2017**, 110, 093503.
- (56) X. He, J. Hu, Z. Zhang, W. Liu, K. Song, J. Meng, Study on the interface electronic properties of AlN (0001)/ β -Ga₂O₃ (100). *Surfaces and Interfaces* **2022**, 28, 101585.
- (57) Z.A. Jian, S. Mohanty, E. Ahmadi, Deep UV-assisted capacitance–voltage characterization of post-deposition annealed Al₂O₃/ β -Ga₂O₃ (001) MOSCAPs. *Applied Physics Letters* **2020**, 116, 242105.
- (58) H. Li, H. Wu, Q. Zhang, C. Tu, Q. Guo, D. Zhai, J. Lu, Study of β -Ga₂O₃ (001)/sapphire (a-plane) heterostructure in wide bandgap solar-blind deep-ultraviolet photodetector. *Journal of Crystal Growth* **2024**, 628, 127513.